Energy Advances

ROYAL SOCIETY OF CHEMISTRY

PAPER

View Article Online
View Journal | View Issue

Check for updates

Cite this: *Energy Adv.*, 2025, 4, 1154

2D layered VSe_2 with high pseudocapacitive Zn-ion storage as a cathode for high-power zinc-ion batteries

Saddam Hussain,[a] Mayanmi Zimik,[a] Meghali Devi,[a] Md Kasif[b] and Ranjith Thangavel *[ab]

Aqueous zinc-ion batteries (ZIBs) are an attractive storage solution for renewable energy storage system (ESS) applications. Despite the intrinsic safety, eco-friendliness, and low cost of aqueous ZIBs, their practical application is severely hindered by the unavailability of high-capacity and robust cathode materials. Vanadium-based cathodes with various structures, large layer spacing, and different oxidation states are considered to be suitable cathode candidates for ZIBs. In this work, we studied 2D layered VSe_2 with high pseudocapacitive-mediated Zn-ion storage as a cathode for aqueous zinc-ion batteries. The VSe_2 cathode reversibly hosted zinc ions with a capacity of 205 mAh g^{-1} at 0.2 A g^{-1}, maintaining a capacity of 135 mAh g^{-1} at 8 A g^{-1} and a stability of 98% after 600 cycles at 1 A g^{-1}, favoured by its 2D layered structure with defects and metallic conducting nature. The Zn-ion storage mechanism and kinetics in the cathode are examined using *ex situ* XRD, XPS, TEM, and GITT studies, and it is found that the favourable interlayer spacing with structural defects efficiently stored Zn-ions through a high contribution from capacitive-mediated storage. The favourable architecture enables fast Zn-ion diffusion and high capacity at a high current rate with good stability. The current work emphasizes the potential for the rational design of several transition-metal–dichalcogenide-based cathodes with strong pseudocapacitive storage for sustainable energy storage systems such as aqueous ZIBs.

Received 13th May 2025,
Accepted 26th July 2025

DOI: 10.1039/d5ya00130g

rsc.li/energy-advances

Open Access Article. Published on 28 July 2025. Downloaded on 4/13/2026 6:53:46 PM.
This article is licensed under a Creative Commons Attribution 3.0 Unported Licence.

1. Introduction

As the world strives for carbon neutrality, the demand for advances in electrochemical energy storage technologies has surged.[1–4] Lithium-ion batteries, which are the most commonly used storage device in portable electronic devices and electric vehicles, have cost limitations due to the scarcity and uneven distribution of Li and Co reserves, and present potential hazards associated with the use of volatile and combustible organic electrolytes.[5,6] The growing demand for energy storage devices for renewable energy storage in grid applications cannot be met by Li-ion batteries. In contrast, aqueous ion batteries are gaining great momentum due to their compatibility with aqueous electrolytes, high ionic conductivity, environmental friendliness, and low cost, making them an ideal solution for large-scale energy storage applications to meet the increasing global energy demands. Since multiple electrons are involved in the redox processes of multivalent metal ions like Al^{3+}, Ca^{2+}, Mg^{2+} and Zn^{2+}, aqueous batteries can theoretically deliver high energy densities. Among the multiple types of aqueous rechargeable batteries, zinc ion batteries (ZIBs) stand out with advantages including low cost, sustainability, increased safety, and high energy density. The utilization of a Zn anode with a superior theoretical capacity of 820 mAh g^{-1} offers high energy density along with excellent chemical stability and durability in aqueous electrolyte, making the system more attractive.[7–11]

Currently, the lack of suitable cathode materials is the primarily limitation in terms of advancements in ZIBs. The unique electrochemistry of Zn places significant restrictions on cathode materials, which must exhibit large capacity while being stable at high voltage. When Zn insertion produces adequate redox kinetics and high ionic/electronic transport in the cathode material and cathode/electrolyte interface, considerable gravimetric power density and rate performance can be observed.[12–15] Again, the structural integrity of the cathode material ensures cyclic stability in ZIBs.

The capacity, energy density, power density, rate performance, and stability of ZIBs are governed by the cathode material. In the past decade, various Mn-based compounds (α,β,γ-MnO_2, $ZnMnO_2$, $KMnO_2$, $MgMn_2O_4$, *etc.*), V-based compounds (vanadium oxides, $Na_3V_2(PO_4)_3$, *etc.*), Prussian blue analogues, and organic

[a] *School of Energy Science and Engineering, Indian Institute of Technology Guwahati, Guwahati, 781039, India. E-mail: ranjith.t@iitg.ac.in*
[b] *Department of Chemical Engineering, Indian Institute of Technology Tirupati, Tirupati, 517619, India. E-mail: ranjith.t@iittp.ac.in*

© 2025 The Author(s). Published by the Royal Society of Chemistry

Open Access Article. Published on 28 July 2025. Downloaded on 4/13/2026 6:53:46 PM. This article is licensed under a Creative Commons Attribution 3.0 Unported Licence.

compounds have been studied as cathode materials for ZIBs.[16] However, the complex structural transformations in manganese-oxide-based cathodes can trigger significant volume changes and a transition to an electrochemically inactive spinel phase, which leads to rapid capacity degradation. Although several polyanion compounds and Prussian blue cathodes exhibited reasonable working potentials, their low specific capacity due to a large-sized structure resulted in low gravimetric energy density. Vanadium-oxide-based cathodes have shown high capacity with favourable 2D structures and fast diffusion. The multiple valence states (V^x, x = 2+, 3+, 4+, 5+) in vanadium-based compounds help to store large amounts of Zn-ions in their structures, delivering high capacity.[5,17,18] Numerous V-based cathode materials including V_xO_y, vanadium phosphates and metal vanadate have shown promising results for Zn-ion battery commercialization. However, the low voltage, 2D structure, and strong electrostatic interactions between the cathode material and divalent Zn ions result in low energy density, sluggish kinetics and poor cyclability.

Recently, layered transition-metal sulfides, which are 2D compounds held together by weak van der Waals forces, have gained significant attention for use in various energy storage devices, including Li-ion batteries, sodium-ion batteries, and supercapacitors. Due to their tunable interlayer spacing and abundant edge sites for Zn-ion storage, the higher polarizability of sulfur anions compared to oxygen anions, and the presence of sulfur vacancies, transition-metal sulfide cathodes have demonstrated high capacity at elevated voltages, along with excellent stability. Several transition metal cathodes based on MS_2 (M = Mo, W, V) have been studied as cathodes for ZIBs, and several strategies including morphology control, structural engineering, surface coating, and composite formation have been employed to improve the electrochemical performance of MS_2 cathodes.

In recent days, exploring transition metal selenide-based materials has gained great momentum. Selenide-based materials that show superior metallic-like electron conductivity and a graphene-like 2D layered structure through van der Waals stacking could allow rapid ion transport and storage. Se ions have a larger atomic radius and weaker electronegativity, making M–Se bonds weaker compared to their M–O and M–S counterparts, which promotes lower polarization and increased reversibility during ion storage. Moreover, the low electronegativity of Se in comparison to O or S reduces the ion migration barrier, enhancing ion/electron transport. Transition metal selenides based on VSe_2, WSe_2, $TiSe_2$, $CuSe_2$, and $MnSe_2$ have recently been explored as potential cathodes for multivalent ion batteries.[19–22]

Among the various transition metal selenides (TMS) that have been explored, VSe_2 is of high interest as it has a naturally large interlayer spacing (0.61 nm) with higher electronic conductivity (1.0×10^3 S m^{-1}) than VS_2 (9.907 S m^{-1}) due to the metallic nature of Se. The electron coupling force between neighbouring V^{4+}–V^{4+} atoms results in metallic features, which, along with the large interlayer spacing, could synergistically provide abundant channels and active sites to store Zn-ions. VSe_2 is emerging as a favourable host material for zinc ions that could deliver high capacity and fast Zn-ion storage in ZIBs.[22–26] However, VSe_2 often faces drawbacks like poor conductivity and low cycle stability when used for energy storage applications, as it is always produced in bulk.[27] The electrochemical performance of TMSs can be optimized using methods like defect engineering, doping and carbon hybrids.[27] TMS–nano-carbon hybrids often provide synergetic advantages by enhancing electronic conductivity and providing abundant internal pores, which improves the electron/ion diffusion kinetics. Multiwalled carbon nanotubes (MWCNT) can impart structural stability with improved conductivity and more efficient ion transfer channels. The unique VSe_2–MWCNT nano-hybrid could facilitate smooth electron transfer by providing pathways for fast electron/ion transfer, thus promoting facile Zn-ion storage.[28,29] Furthermore, the Zn-ion storage mechanism in transition metal selenides is poorly understood and requires deeper investigation.

Herein, we propose a VSe_2–MWCNT composite as a cathode material to host Zn^{2+} ions in an aqueous Zn-ion battery. This work aims to incisively ameliorate the structural and electrochemical properties of VSe_2 nanosheets *via* the incorporation of MWCNTs for reversible Zn-ion storage. Although VSe_2-based cathode materials for Zn-ion batteries have been studied previously, we demonstrate a rationally designed VSe_2–MWCNT hybrid composite and investigate the Zn-ion storage mechanism in depth. The hybrid architecture containing 2D layered VSe_2 over 1D multi-walled CNTs synergistically overcomes the intrinsic restacking and conductivity limitations of pristine VSe_2. Furthermore, the abundant selenium vacancy sites promote reversible Zn^{2+} intercalation, providing new insights into defect-assisted fast pseudocapacitive storage (92.62% at 0.5 mV s^{-1}) in layered selenides. The synergy of the two-dimensional VSe_2 nanosheets and MWCNTs results in a superior capacity of 205 mAh g^{-1} at 0.2 A g^{-1}.

In this work, we have studied the few-layered VSe_2–MWCNT nano-hybrid as a cathode material to host Zn^{2+} ions in an aqueous Zn-ion battery. The synergistic effect of the few-layered VSe_2 nanosheets with the MWCNTs in the nano-hybrid results in superior reversibility, with a capacity of ~208, 205, 198, 185, 168, and 134 mAh g^{-1} at 0.2, 0.4, 1, 2, 4, and 8 A g^{-1}, respectively. The high-rate capability with high stability is favoured by the 2D layered structure with defects and a metallic conducting nature, and surpasses many previously reported vanadium-based cathodes. Further in-depth investigation of the Zn-ion storage mechanism using *ex situ* XRD, XPS, TEM, and GITT revealed that the favorable 2D layered structure in the transition metal selenides with a large interlayer distance exhibited pseudocapacitive-type intercalation storage in the Zn-ion battery.

2. Experimental section

2.1. Synthesis of VSe_2 and VSe_2–MWCNT

VSe_2 nanoflakes were synthesized *via* a one-step hydrothermal method. 1 mmol of vanadium pentoxide (V_2O_5) and 4 mmol of selenium dioxide (SeO_2) were thoroughly dispersed in DI water under constant stirring. This was followed by the gradual

Open Access Article. Published on 28 July 2025. Downloaded on 4/13/2026 6:53:46 PM. This article is licensed under a Creative Commons Attribution 3.0 Unported Licence.

addition of 19.5 mmol of oxalic acid ($C_2O_4H_2$), and the mixture was hydrothermally treated at 200 °C for 24 h using a Teflon-lined stainless-steel autoclave. The VSe_2 powders were collected by centrifugation, thoroughly washed with DI water and acetone, and dried using a vacuum oven at 60 °C for 6 h. For the synthesis of the VSe_2–MWCNT composite, an aqueous dispersion of 5 wt% MWCNT was added to the mixture under stirring; all other procedures remained the same. An MWCNT dispersion in DI water purchased from a local vendor was used without any pretreatment. The MWCNTs were again dispersed in DI water using a probe sonicator for 30 min.

2.2. Physical characterization

The crystal structure of the synthesized materials was studied with an X-ray diffractometer (Rigaku Smart Lab, X-ray source Cu Kα, λ = 1.54 Å) at a scan rate of 5° min^{-1}. The surface morphology and microstructure of the materials were analysed with a field emission scanning electron microscope (Sigma 300) at 5 kV and a field emission transmission electron microscope (JEOL, JEM-2100F) with an operating voltage of 200 kV. The SAED patterns of the synthesized materials were also obtained using the JEOL JEM-2100F instrument. The surface chemical environment was evaluated *via* X-ray photoelectron spectroscopy (XPS) with an ESCALAB Xi+ (Thermo Fisher Scientific, X-ray source: Al Kα). A laser micro Raman system with a wavelength of 633 nm (Horiba Jobin Vyon, Model: LabRam HR) was used to perform Raman spectroscopy. A high-temperature differential scanning calorimetry (DSC)/thermogravimetric (TG) system (Netzsch Model: STA449F3A00) was used to perform thermogravimetric analysis (TGA).

2.3. Electrochemical characterization

A homogeneous cathode slurry was prepared with VSe_2@MWCNT, carbon black and PVDF in an 8 : 1 : 1 weight ratio in the solvent NMP and cast over stainless-steel (SS) foil using a doctor blade. The slurry-coated SS foil was further vacuum dried at 60 °C. A Zn foil with a diameter 12 mm was used as a counter electrode to investigate the electrochemical performance in a CR-2032 coin cell assembled under ambient conditions utilising 3 M $Zn(CF_3SO_3)_2$ aqueous electrolyte. The mass loading of the cathode was ~2.5 mg cm^{-2}, and the diameter of the cathode was 12 mm. All electrochemical characterisations were carried out using an Origalys Workstation.

3. Results and discussion

3.1. Physical characterizations

The X-ray diffraction pattern of VSe_2 in Fig. 1a shows a crystalline structure and confirms the pure phase details of the VSe_2 and VSe_2–MWCNT hybrids (JCPDS file No. 89-1641). The VSe_2 pattern is attributed to a hexagonal crystal structure with the space group $P\bar{3}ml$, and the calculated lattice parameters were $a = b$ = 0.336 nm, c = 0.611 nm. The XRD patterns of VSe_2–MWCNT hybrids have an additional peak at $2\theta = 26°$ due to the (002) plane after incorporation of the CNTs. The Raman spectra of the VSe_2 cathode in Fig. 1b shows two peaks centred around 145 cm^{-1} (E_{2g}) and 205 cm^{-1} (A_{1g}), which correspond to the first-order in-plane atomic vibrations inside the Se–V layers and out-of-plane perpendicular vibration modes of the Se layers. The E_{2g} and A_{1g} peaks in VSe_2–MWCNT are shifted to higher wavenumber due to the lattice distortion and selenium vacancies due to the few-layered morphology and highly conductive MWCNT network.[24,30,31] The MWCNTs present in the VSe_2 nanohybrid displayed the typical D band of carbon at 1326 cm^{-1} and G band at 1587 cm^{-1} in the Raman spectrum. The I_D/I_G ratio of 1.63 in the VSe_2–MWCNT nanohybrid indicates a higher defect density in the hybrid. The presence of a layered structure along with defects in the 2D layered VSe_2–MWCNT nanohybrid could provide abundant active sites for Zn-ion storage, enhanced Zn-ion diffusion, and a strong interface.[32] The hybrid architecture can control particle detachment by immobilizing the VSe_2 sites during the volume changes associated with Zn-ion (de)intercalation and thus increase the stability and rate capability of the hybrid.

The TGA analyses of the VSe_2 and VSe_2–MWCNT composite in Fig. S1 show the change in weight as a function of temperature, and were used to evaluate their thermal stability as well as the weight% of MWCNT in the composite. For both materials, an initial weight loss with the evaporation of chemisorbed water was observed around 100 °C, and at ~200 °C, the weight of VSe_2@MWCNT increased slightly. The functional groups present in the porous MWCNTs may facilitate the oxidation of VSe_2. As MWCNT–VSe_2 hybrid has high surface area, at ~200 °C, oxygen can chemisorb onto the defect sites or edges, leading to a slight mass increase.[33] A steep weight loss was observed between 375 °C and 525 °C. The VSe_2 material did not show any weight loss above 525 °C; however, the VSe_2–MWCNT composite material exhibited an 8.8% weight loss, which was attributed to the decomposition of the carbonaceous framework of the MWCNT. The field emission scanning electron microscopy (FE-SEM) images of pristine VSe_2 (Fig. S2a and b) show a nanoplate morphology with a thickness of ~5 nm, forming a hierarchical spherical flower-like morphology. However, the FE-SEM image of the VSe_2–MWCNT nanohybrids (Fig. 1c and d) shows densely packed and non-agglomerated VSe_2 particles over CNT sheets. The severe particle agglomeration was strongly inhibited by the presence of the conductive CNT network. The VSe_2–MWCNT nanohybrids display evenly dispersed MWCNTs interconnecting the VSe_2 flakes. This interlinked network of VSe_2 flakes in the MWCNT hybrids favors rapid electron transfer through the hybrid cathode material, enhancing material utilization at high current rates. This hierarchical flower-like surface morphology ensures the enhanced participation of more redox active sites for Zn-ion (de)intercalation with increased surface area. Fig. 1e and f and Fig. S2c show the FETEM image, in which the 2D sheet-like morphology of VSe_2 with diameters of ~500 to 600 nm is evident. The HR-TEM images of the VSe_2–MWCNT nanohybrids (Fig. 1g) clearly show the lattice fringes, confirming its highly crystalline nature with a d-spacing of 0.61 nm (inset: Fig. 1g), corresponding to the (002) plane of VSe_2. The elemental mapping of VSe_2–MWCNT (Fig. S2d) using the HAADF technique shows the

 © 2025 The Author(s). Published by the Royal Society of Chemistry

Open Access Article. Published on 28 July 2025. Downloaded on 4/13/2026 6:53:46 PM.
This article is licensed under a Creative Commons Attribution 3.0 Unported Licence.

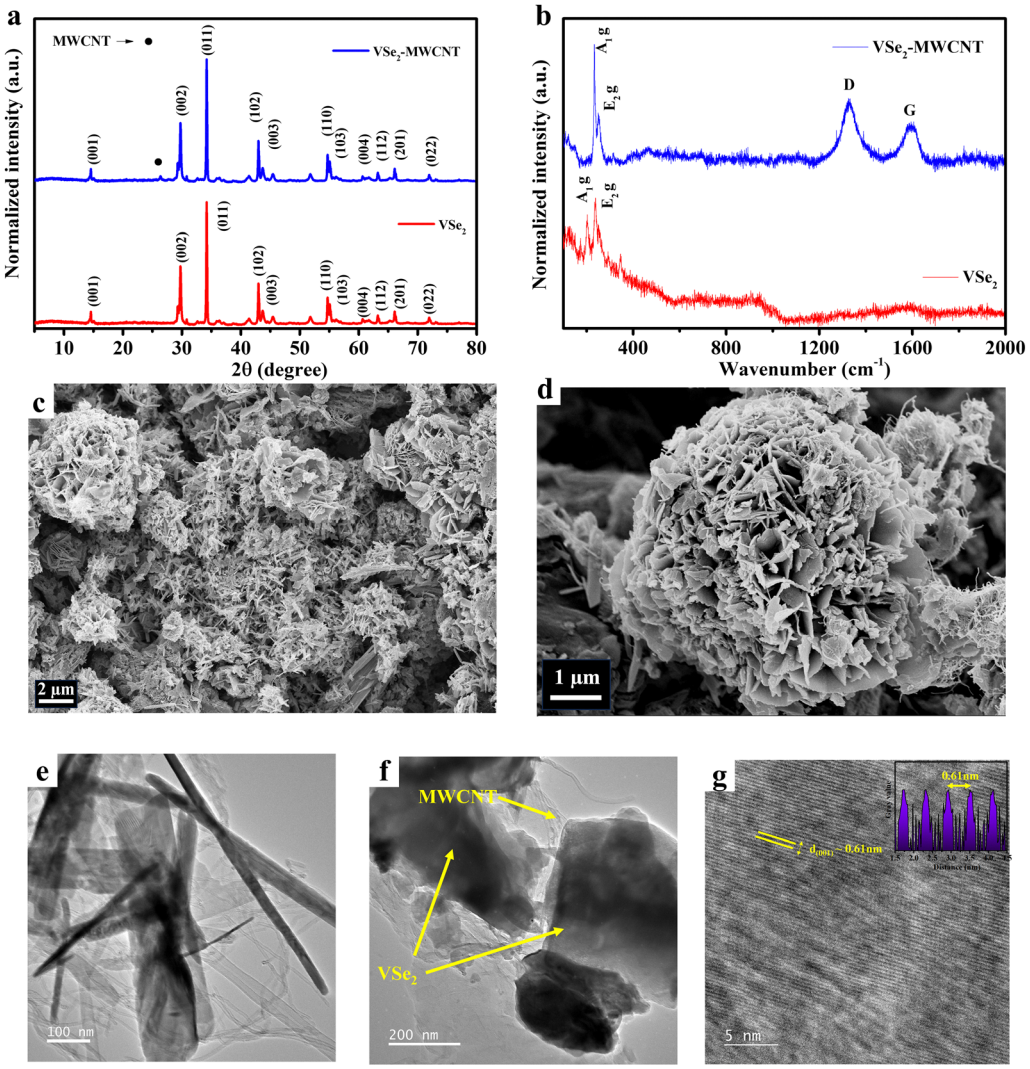

Fig. 1 (a) XRD plots of VSe_2 and VSe_2–MWCNT hybrid. (b) Raman spectra of VSe_2 and VSe_2–MWCNT hybrid. (c) and (d) FESEM images of VSe_2–MWCNT hybrids. (e) and (f) TEM images of VSe_2–MWCNT hybrid and (g) HR-TEM image of VSe_2–MWCNT.

uniform distribution of the elements V, Se and C, as presented in Fig. 2d–g.

The surface chemical environment of the VSe_2–MWCNT composite material was analysed using the XPS technique. The presence of the elements V, Se and C was confirmed from the XPS survey spectrum, as shown in Fig. 2a. In Fig. 2b, the characteristic peaks for V^{4+} $2p_{1/2}$ and V^{4+} $2p_{3/2}$ are observed at 524 eV and 517.8 eV in the deconvoluted spectrum of V 2p. V^{4+}-based vanadium materials tend to have metallic properties with more favorable electron transport behaviour during cycling than V^{5+}-based vanadium phases, which are insulating or semi-conducting. This facilitates reversible redox reactions during Zn-ion storage and better structural stability during repeated intercalation and deintercalation. Moreover, vanadium compounds with V^{4+} to V^{3+} redox show open frameworks, helping to accommodate Zn-ions without structural degradation. However, vanadium compounds with V^{5+}-to-V^{4+} redox can suffer from structural distortion.[34] This can be correlated to the effects of phase transition during the redox process, which are crucial for capacity retention in sodium-ion and lithium-ion batteries.[35,36] Some V^{3+} is also observed in the compound, indicating the presence of defects in the VSe_2 cathode, which could be attributed to Se vacancies or intrinsic electron distribution. Such defects are beneficial for Zn-ion storage, as the defects could lower the Zn^{2+} insertion energy barrier and provide diffusion channels or interstitial sites for more Zn-ion storage.[20] The deconvoluted Se 3d spectrum in Fig. 2c shows the characteristic peak for Se $3d_{3/2}$ and Se $3d_{5/2}$ at binding energies of 55.2 eV and 56.3 eV.[32,37] The C 1s spectrum can be deconvoluted (Fig. 2d) into C–C bonds (285.1 eV), C–O bonds (285.1 eV), and C═O bonds (290.43 eV). The presence of C–O interactions in the composite material increases the electrode wettability towards the electrolyte with increased hydrophilicity for efficient charge storage with the VSe_2–MWCNT composite material. Along with the peak for sp^2-hybridized C atoms, another satellite peak due to the graphitic nature of the

Open Access Article. Published on 28 July 2025. Downloaded on 4/13/2026 6:53:46 PM.
This article is licensed under a Creative Commons Attribution 3.0 Unported Licence.

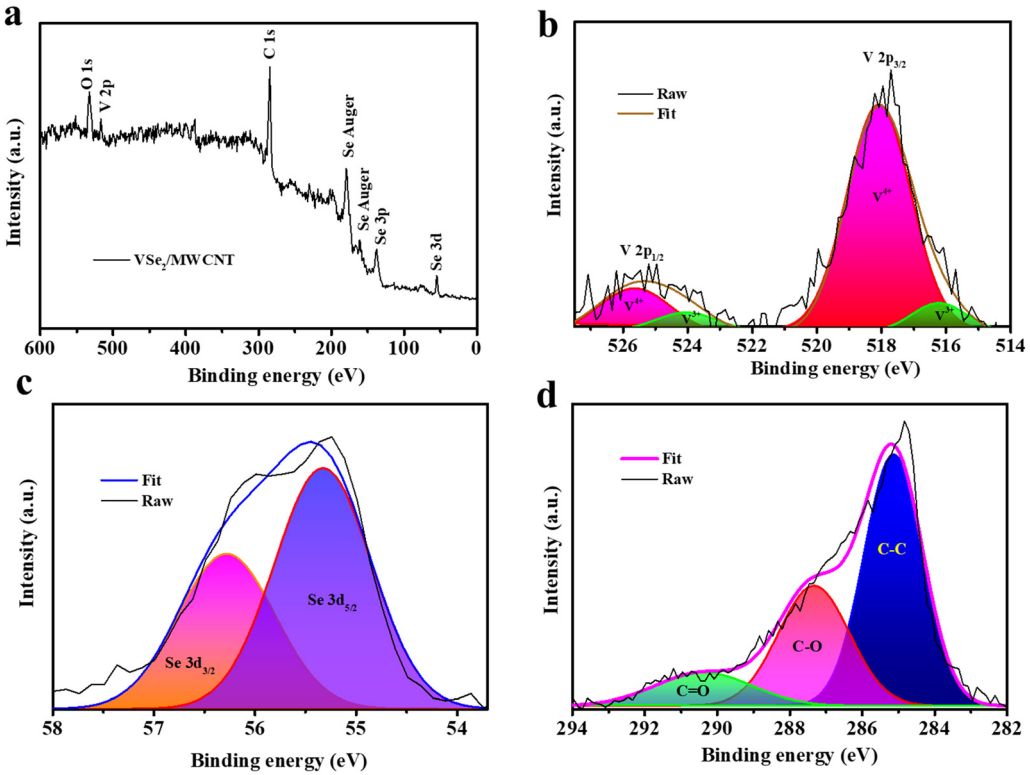

Fig. 2 (a) Full-scale survey for VSe_2–MWCNT. Magnified and deconvoluted XPS spectra: (b) V 2p peak, (c) Se 3d, and (d) C 1s peak.

MWCNTs is observed, which confirms the structural intactness of the MWCNTs in the composite.[30,31] The MWCNTs can offer structural stability to the composite during charge/discharge, as well as facilitate Zn ion intercalation in the VSe_2 layers. Again, the incorporation of highly conductive MWCNT in the composite adds porous conducting channels and surface defects to the layered VSe_2 architecture for a reduced diffusion distance for Zn ions and allows enhanced influx of Zn ions in a brief period.[24,38] This design is promising to diminish interfacial resistance and increase the electrode–electrolyte interfacial area.

3.2. Electrochemical characterization

The electrochemical performance of the pristine VSe_2 and the VSe_2–MWCNT nanohybrid cathodes was systematically evaluated through cyclic voltammetry (CV) and galvanostatic charge–discharge (GCD) studies in the voltage window of 0.2–1.6 V. Fig. 3a compares the CV curves of pristine VSe_2 and VSe_2–MWCNT at 0.5 mV s^{-1}. The CV curves of the VSe_2–MWCNT nanohybrid show sharper and more intense redox peaks with smaller polarization than pristine VSe_2, indicating faster Zn^{2+} insertion/extraction kinetics along with enhanced electrochemical reversibility. The incorporation of the MWCNT network effectively improves the electronic conductivity of VSe_2, enhancing the active material utilization for Zn-ion storage. The GCD curves in Fig. 3b clearly demonstrate the superior electrochemical behaviour of the VSe_2–MWCNT nanohybrid compared to pristine VSe_2. The VSe_2–MWCNT nanohybrid shows a discharge capacity of 214 mAh g^{-1} at 0.4 A g^{-1}, while pristine VSe_2 showed a capacity of only ~140 mAh g^{-1}. The hybrid cathode delivers a higher specific discharge capacity with more defined voltage plateaus and lower polarization than pristine VSe_2, confirming improved Zn-ion storage, enhanced charge transfer kinetics and reduced internal resistance.[39] During the discharge process, the VSe_2–MWCNT nanohybrid cathode exhibits well-defined plateaus at 0.9 V and 0.55 V corresponding to Zn-ion intercalation into the VSe_2 structure *via* the reduction of V^{4+} ions to form the zinc intercalated compound Zn_xVSe_2. The plateaus at 0.71 V and 1.1 V upon consecutive charging correspond to the oxidation step of the Zn_xVSe_2 to form VSe_2 during the Zn-ion deintercalation process. The enhanced redox kinetics, decreased polarization, and enhanced capacity are also reflected as a reduced potential difference between the charging and discharging plateaus ($\Delta E \sim 0.44$ V). The highly reversible nature of Zn-ion storage in the VSe_2–MWCNT nanohybrid can be further validated with consecutive CV curves. The shape profile of the CV curves remained similar, and the highly overlapping CV curves with negligible polarization even after 5 cycles (Fig. 3c) indicate excellent electrochemical reversibility, with strong stability during repeated Zn-ion intercalation/deintercalation processes. The cathodic peaks observed in the CV curves at 0.66 V and 1.1 V are attributed to the following reactions:[16]

$$VSe_2\text{–MWCNT} + mZn^{2+} + 2me^- \leftrightarrow Zn_mVSe_2\text{–MWCNT}$$

$$Zn_mVSe_2\text{–MWCNT} + nZn^{2+} + 2ne^- \leftrightarrow Zn_{(m+n)}\,VSe_2\text{–MWCNT}$$

© 2025 The Author(s). Published by the Royal Society of Chemistry

Open Access Article. Published on 28 July 2025. Downloaded on 4/13/2026 6:53:46 PM.
This article is licensed under a Creative Commons Attribution 3.0 Unported Licence.

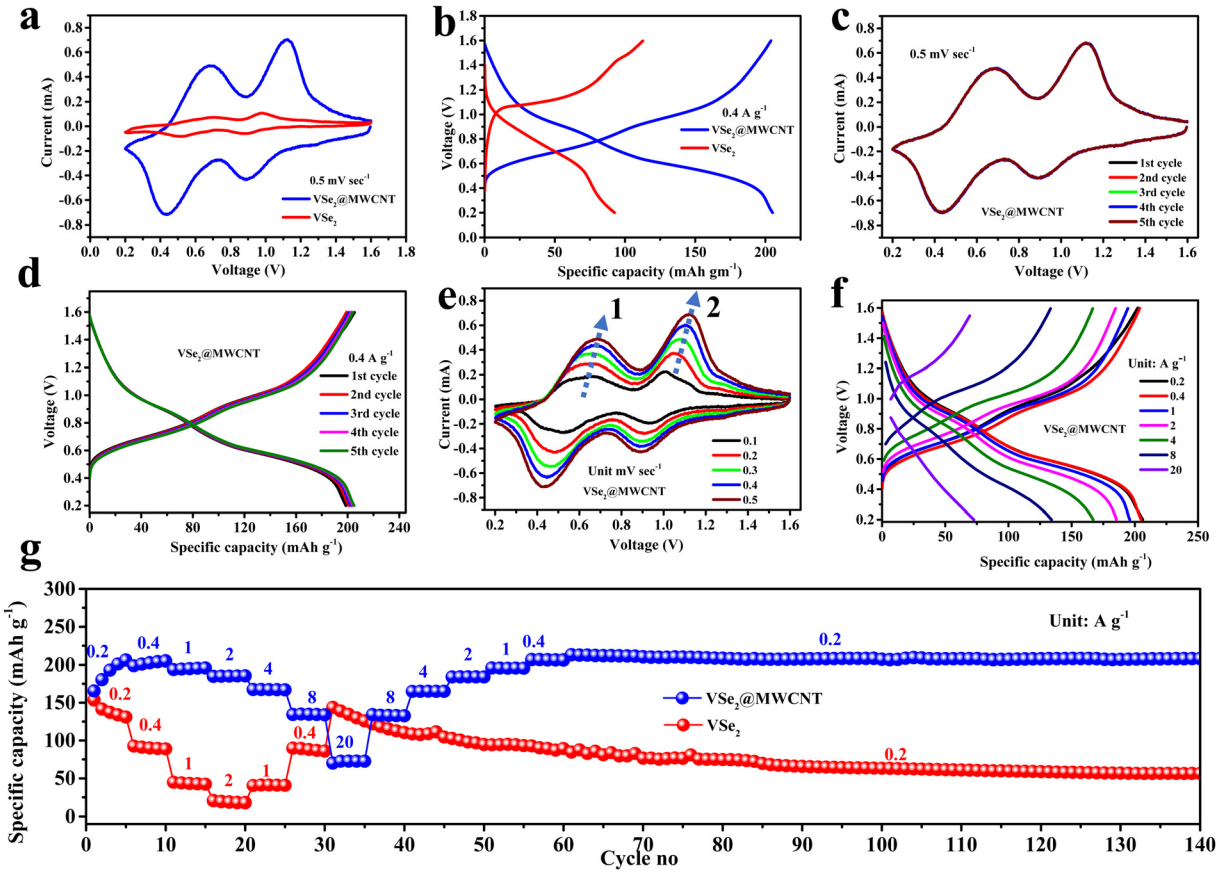

Fig. 3 Electrochemical performance: (a) cyclic voltammetry (CV) curves at 0.5 mV s^{-1} and (b) galvanostatic charge–discharge (GCD) plot. (c) CV curves of VSe_2–MWCNT at different cycles (0.5 mV s^{-1}). (d) CV curves of VSe_2–MWCNT at different scan rates. (e) GCD curves at 0.4 A g^{-1} and (f) GCD curves at different current densities. (g) Rate performance of VSe_2–MWCNT and pristine VSe_2 cathodes.

The shape profiles of the CV curves and the redox peak position remained unchanged even after the scan rate was increased to 0.5 mV s^{-1} from 0.1 mV s^{-1} (Fig. 3d), indicating superior electrochemical resilience in the VSe_2–MWCNT nano-hybrid. The highly reversible nature of the VSe_2–MWCNT nano-hybrid is shown by the nearly intact charge–discharge curves at 0.2 A g^{-1}, as shown in Fig. 3e, which signifies the highly reversible nature of Zn-ion storage in the cathode. Meanwhile, the GCD curves show two clearly distinguishable discharge plateaus, corresponding to the two pairs of redox peaks in the CV curves, implying the existence of a two-step Zn-ion insertion/removal process. However, the GCD curves of pristine VSe_2 (Fig. S3a) exhibit lower capacity and more rapid capacity decay upon consecutive cycles than the VSe_2–MWCNT nano-hybrid. The polarization of the charge–discharge curves is also higher than that of the VSe_2–MWCNT nano-hybrid. The favourable structure of the VSe_2 and MWCNT composite exhibits improved discharge capacity, coulombic efficiency, and polarization, indicating prompt and reversible Zn-ion storage in the VSe_2 cathode.

The rate capability of the composite cathode materials was examined to ensure their applicability in high-power applications. The VSe_2–MWCNT nano-hybrid showed excellent rate cyclability (Fig. 3f and g) with a maximum specific capacity of 208 mAh g^{-1} at 0.2 A g^{-1} and retains a capacity of ~208, 205, 198, 185, 168, and 134 mAh g^{-1} at 0.2, 0.4, 1, 2, 4, and 8 A g^{-1}, respectively. Further, when the current rate was reverted to 0.2 A g^{-1}, VSe_2–MWCNT demonstrated a remarkable capacity recovery, delivering a capacity of over ~213 mAh g^{-1}. This observation implies the structural integrity of the VSe_2–MWCNT composite cathode under dynamic electrochemical conditions.[40] In contrast, the pristine VSe_2 cathode provides a specific capacity of 150 mAh g^{-1} at 0.2 A g^{-1}, which decays to 20 mAh g^{-1} at a higher current rate of 2 A g^{-1}, as shown in Fig. S3b. The lower capacity, higher polarization and poor capacity recovery at lower current density in the pristine cathode are mainly due to the poor electronic conductivity of the cathode without the carbon network. As researchers worldwide have been searching for a suitable cathode material with high capacity and structural stability under dynamic electrochemical conditions, the current work on VSe_2–MWCNT represents a promising result in comparison to recently explored cathodes such as α,β,γ-MnO_2, V_2O_5, NaV_3O_8, PANI-CFs, TMD cathodes like VS_2 and VS_2–rGO, *etc.*[41,42] Along with the conductivity and defect sites provided by the narrow 2D structure, the well-dispersed and lamellar VSe_2 structure is responsible for the superior rate performance of the composite cathode. The rational design of the VSe_2–MWCNT cathode ensures

Open Access Article. Published on 28 July 2025. Downloaded on 4/13/2026 6:53:46 PM.
This article is licensed under a Creative Commons Attribution 3.0 Unported Licence.

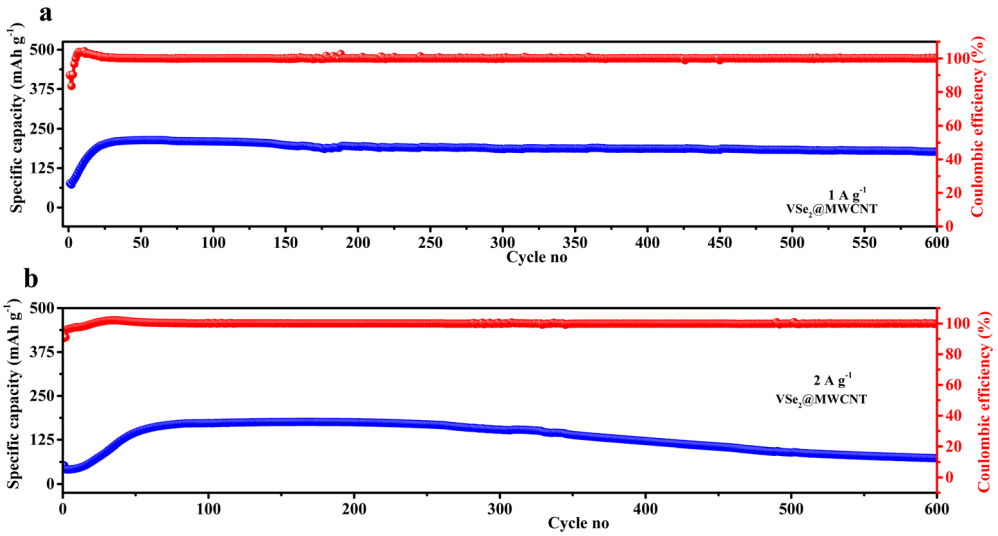

Fig. 4 Long-term cyclic stability of the VSe_2–MWCNT cathode at (a) 1 A g^{-1} and (b) 2 A g^{-1}.

decreased polarization and rapid charge transfer between the 2D stacked VSe_2 layers and MWCNT for exceptional rate performance. Moreover, the few-layered VSe_2 and MWCNT composite is able to withstand mechanical stress or strain during rapid Zn ion exchange under high-current-rate conditions.

The long-term cyclability of the VSe_2 cathode was tested at a lower current rate (1 A g^{-1}) as well as at a higher current rate (2 A g^{-1}), and the results are presented in Fig. 4. The VSe_2–MWCNT nanohybrids display incredible stability along with excellent coulombic efficiency even after 600 cycles when tested at 1 A g^{-1}. This suggests the synergistic effect of the MWCNTs with VSe_2 in terms of structural integrity during repeated Zn-ion insertion and extraction processes, as well as enhanced electrochemical activity.[43,44] When tested at 2 A g^{-1} (Fig. 4b), the VSe_2–MWCNT nano-hybrid cathode showed a stable capacity (600 cycles) after the initial capacity stabilization process. The initial structural stabilization in the VSe_2 cathode due to the higher charge density and larger size of Zn^{2+} ions could contribute to the slow increase in the initial capacity; this aspect requires further investigation.[45–47] The VSe_2–MWCNT initially shows increasing capacity, and the capacity becomes almost constant at 185 mAh g^{-1} after 50 cycles. The coulombic efficiency of the composite cathode also remained the same, indicating highly reversible Zn ion storage. This is attributed to the defects introduced by the MWCNTs, which can also serve as additional sites for Zn absorption.[48] At the higher current density of 2 A g^{-1}, a slight decline in capacity after 300 cycles is observed compared to the cyclic stability at 1 A g^{-1}. Higher current rates will lead to more severe surface reactions due to unwanted electrolyte decomposition, forming resistance layers. The new layers could block ion access and increase the internal resistance, resulting in quick capacity fade. Increased overpotential and polarization due to higher internal resistance will trigger quick capacity fading at higher current. During long-term cycling, high mechanical stress during zinc ion insertion and extraction at a high current rate will lead to cracking and degradation of the electrodes.[49] Table S1 compares the performance of the VSe_2–MWCNT cathode to those of several recently reported vanadium- and transition-metal-based cathodes for ZIBs. It is clearly seen that the VSe_2–MWCNT cathode outperforms most of the recently studied vanadium- and transition-metal-based cathodes. VSe_2–MWCNT showed higher capacity, superior rate performance, and longer-term stability than the other cathodes. The VSe_2–MWCNT exhibits superior performance, mainly due to the synergistic effect of the 2D-structured VSe_2 grown over the 1D-structured MWCNTs.

The Nyquist impedance plots for the VSe_2 and VSe_2–MWCNT cathodes over the frequency range of 10 mHz–100 kHz are shown in Fig. S4. In the high-frequency range, a semicircle is observed, which corresponds to the charge transfer resistance (R_{ct}). In the low-frequency range, the inclined line represents the Warburg impedance (W_0). The resistance originating from the electrolyte and cathode material interface along the line from the origin to the intersection point of the semicircle along the real axis is the ohmic resistance (R_0). With the addition of MWCNTs, the diameter of the semi-circle, and thus the charge transfer resistance (R_{ct}), decreases, and the length of the inclined line increases. This implies more rapid diffusion of Zn-ions through the cathode material in the VSe_2–MWCNT nano-hybrid than in VSe_2. VSe_2–MWCNT exhibits an ohmic resistance (R_0) of approximately 1.4 Ω and a charge transfer resistance of around 43 Ω. In contrast, pristine VSe_2 displays an ohmic resistance (R_0) of 18 Ω and a charge transfer resistance (R_{ct}) of about 182 Ω. The low R_{ct} and R_0 are attributed to the synergy of the VSe_2 2D sheets and the MWCNT conductive network to boost the storage kinetics.[50]

The gravimetric intermittent titration technique (GITT) was utilized to quantitatively examine the Zn-ion diffusion kinetics with transient voltage change in the VSe_2–MWCNT nanohybrid cathode. This technique involves applying quick charging/discharging pulses of 10 min followed by a longer relaxation time of 2 h to attain equilibrium; this process is repeated until

© 2025 The Author(s). Published by the Royal Society of Chemistry

Open Access Article. Published on 28 July 2025. Downloaded on 4/13/2026 6:53:46 PM.
This article is licensed under a Creative Commons Attribution 3.0 Unported Licence.

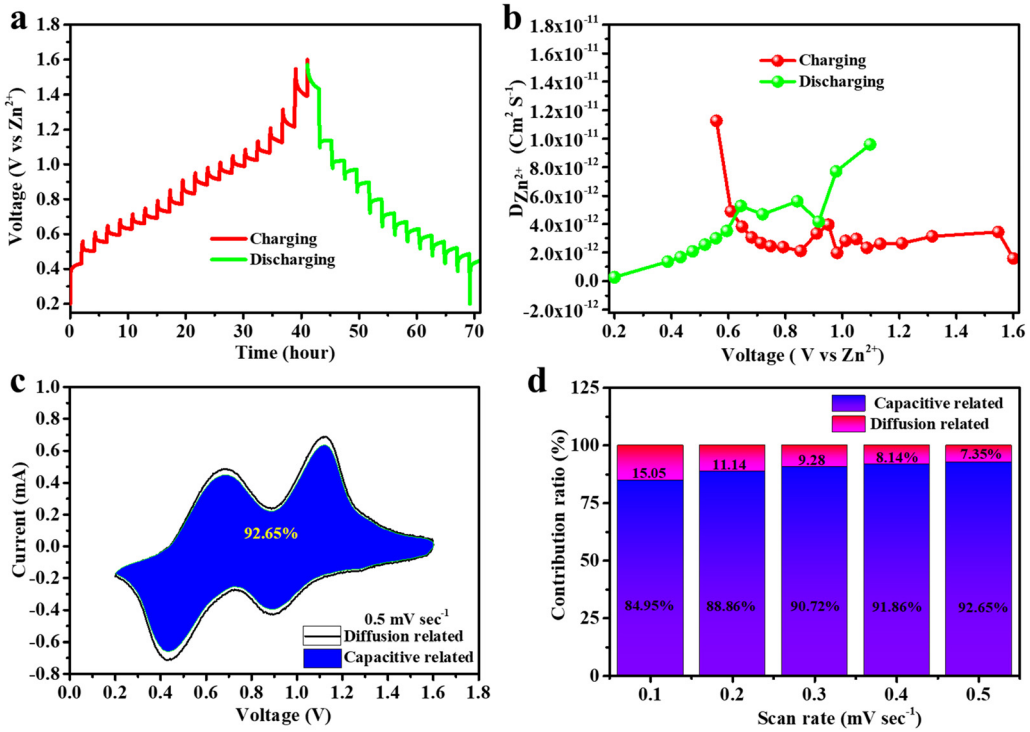

Fig. 5 (a) GITT: voltage *vs.* time plot of the VSe_2–MWCNT nanohybrid, (b) diffusivity *vs.* voltage plot of VSe_2–MWCNT, (c) capacitive contribution of VSe_2–MWCNT at a scan rate of 0.5 mV s^{-1} and (d) capacitive and diffusive contributions at different scan rates for VSe_2–MWCNT.

the full charge/discharge window is covered. The Zn-ion diffusion coefficient during the intercalation/deintercalation process can be calculated using Fick's second law as $D_{Zn} = 4/\pi\tau(m_B V_M/M_W A)_2$-$(\Delta E_S/\Delta E_\tau)$, where m_B, V_M, and M_W are the mass, molar volume, and molecular weight of the VSe_2 cathode, respectively, τ is the time of the applied galvanostatic current (s), A is the specific area of the cathode (cm^2), and ΔE_S and ΔE_τ are the pseudo-equilibrium voltage and voltage change during the current pulse (V), respectively. Fig. 5a and b displays the equilibrium voltage for the different Zn-ion intercalation/deintercalation steps, and the corresponding Zn-ion diffusion coefficients. During the discharge phase, the maximum Zn-ion diffusion coefficient derived using Fick's second law was 9.74×10^{-12} cm^2 s^{-1} for the VSe_2–MWCNT nanohybrid.[51] The presence of a porous channel network of MWCNTs between the two-dimensional VSe_2 sheets facilitates the prompt diffusion of Zn^{2+} ions inside the cathode materials, which reduces the intrinsic resistance of the cathode.[39,52] Interestingly, the VSe_2–MWCNT composite cathode exhibited a higher Zn-ion diffusion co-efficient than previously studied metal–oxide, metal–sulfide-, and polyanion-based cathodes.[53–57] The synergy between the metallic VSe_2 and carbonaceous MWCNTs offers a higher active surface area and electron-ion intercalation and deintercalation, which speeds interfacial charge transfer and minimises undesirable reactions at the cathode side.[30,58–61] The MWCNTs eliminate constraints related to Zn-ion diffusion and result in exceptional electrochemical performances at greater current and power densities.

The rapid Zn-ion storage kinetics of the VSe_2–MWCNT nanohybrid cathode were studied using the current–voltage relationship obtained from the CV measurements previously taken at different scan rates ranging from 0.1 mV s^{-1} to 0.5 mV s^{-1}. The capacitive and diffusion-related reaction kinetics can be represented using the equation[51,62] $i = a_1\nu + b_2\nu^{1/2}$. Here, $a_1\nu$ is the capacitive contribution to ion storage, and $b_2\nu^{1/2}$ represents the diffusion-influenced reaction kinetics at a specific scan rate. At a scan rate of 0.5 mV s^{-1}, the capacitive and diffusive current contributions for the VSe_2–MWCNT nanohybrid were calculated to be ~92.65% and 7.35%, respectively (Fig. 5c). Fig. 5d displays a histogram of the percentage of capacitive and diffusive current contributions at scan rates ranging from 0.1 to 0.5 mV s^{-1}. It is notable that the capacitive current contribution intensified with increasing the scan rate from 0.1 to 0.5 mV s^{-1}, with the capacitive contribution being 88.86%, 90.72%, 91.86%, and 92.65% at 0.2, 0.3, 0.4, and 0.5 mV s^{-1} respectively. The log(peak current) *vs.* log(scan rate) analysis (Fig. S5a) provided the b values for peak-1 and peak-2 at 0.59 and 1.04 V, respectively, indicating a combination of diffusion and surface-controlled processes, with the latter Zn-ion storage peak dominating. At 0.5 mV s^{-1}, the VSe_2–MWCNT composite exhibited a capacitive contribution of 92.65% (Fig. 5c) with excellent linearity (R_1^2 = 0.998, R_2^2 = 0.994) being observed at all the analysed voltages. To further support the capacitive storage behaviour in the VSe_2–MWCNT nanohybrid cathode, we reconsidered the CV analysis and compared the pseudocapacitive behaviour of pristine VSe_2, pristine MWCNTs, physically mixed VSe_2–MWCNTs, and the hydrothermally produced VSe_2–MWCNT nanohybrid. The pristine VSe_2 showed a capacitive contribution of 28.16%

Open Access Article. Published on 28 July 2025. Downloaded on 4/13/2026 6:53:46 PM.
This article is licensed under a Creative Commons Attribution 3.0 Unported Licence.

for Zn-ion storage (Fig. S5b), which was much lower than that of the VSe_2–MWCNT nanohybrid (92.65%) (Fig. 5c). The pristine MWCNTs showed EDLC-type storage behaviour with a pseudocapacitive contribution of 85.60% (Fig. S5c), while the physically mixed VSe_2 and MWCNTs showed a pseudocapacitive contribution of only 73.07% (Fig. S5d). These findings clearly demonstrate the superior capacitive performance of the composite, which can be attributed to the synergistic interaction between VSe_2 and MWCNTs. The hybrid architecture containing 2D layered VSe_2 over 1D multi-walled CNTs synergistically overcame the intrinsic restacking and conductivity limitations of pristine VSe_2 to improve the electrochemical kinetics and significantly boost the capacitive behaviour. The unique 2D layered structure of VSe_2 facilitates easy ion diffusion between the layers and allows rapid electron transfer, while the MWCNTs have high inherent electronic conductivity and high surface area. The synergy in the composite leads to enhanced ion diffusion, which contributes to high pseudocapacitance. The presence of defect sites in VSe_2 also increases the amount of active sites for Zn-ion storage, promoting surface-controlled redox reactions and thereby increasing the overall pseudocapacitance. The high mechanical strength of the MWCNTs helps to prevent any mechanical degradation, which in turn promotes the retention of the pseudocapacitance during long cycling. The structure also favoured fast ion adsorption due to effective interface contact with the electrolyte, helping to achieve high capacity at high current rates. The large buffer space generated in the MWCNT-2D VSe_2 sheets can minimize severe volume changes during the charge/discharge cycles and offer an efficient pathway for Zn-ion flux at the electrode/electrolyte interface.[51]

Fig. 6a shows the *ex situ* XRD patterns of the VSe_2–MWCNT nanohybrid during zinc ion storage at different states of charge, giving good insight into the structural changes associated with the VSe_2 cathode during Zn-ion (de)intercalation. Fig. 6b–e show magnifications of the peaks of the (001) plane, MWCNTs, (002) plane, and (011) plane in the *ex situ* XRD pattern. The continuous peak shifting followed by peak recovery suggest that the VSe_2 can accommodate and release Zn ions without complete structural collapse.[34,63] Fig. 6c shows the XRD peak for zinc hydroxide, which is a common by-product formed in vanadium-based cathodes during battery cycling, along with the peaks corresponding to the MWCNTs. In an aqueous electrolyte, the local environment around the electrolyte can become more alkaline due to the movement of hydroxide ions (OH^-), which can react with zinc ions to form the by-product zinc hydroxide ($Zn(OH)_2$). The XRD patterns shows the reversible Zn^{2+} intercalation storage in VSe_2 with associated crystalline structural changes, indicating VSe_2 as a potential cathode for ZIBs. During the charge/discharge process, possible electrolyte diffusion and zinc-ion insertion/extraction into the MWCNTs will alter the interplanar spacing of the MWCNTs, leading to peak

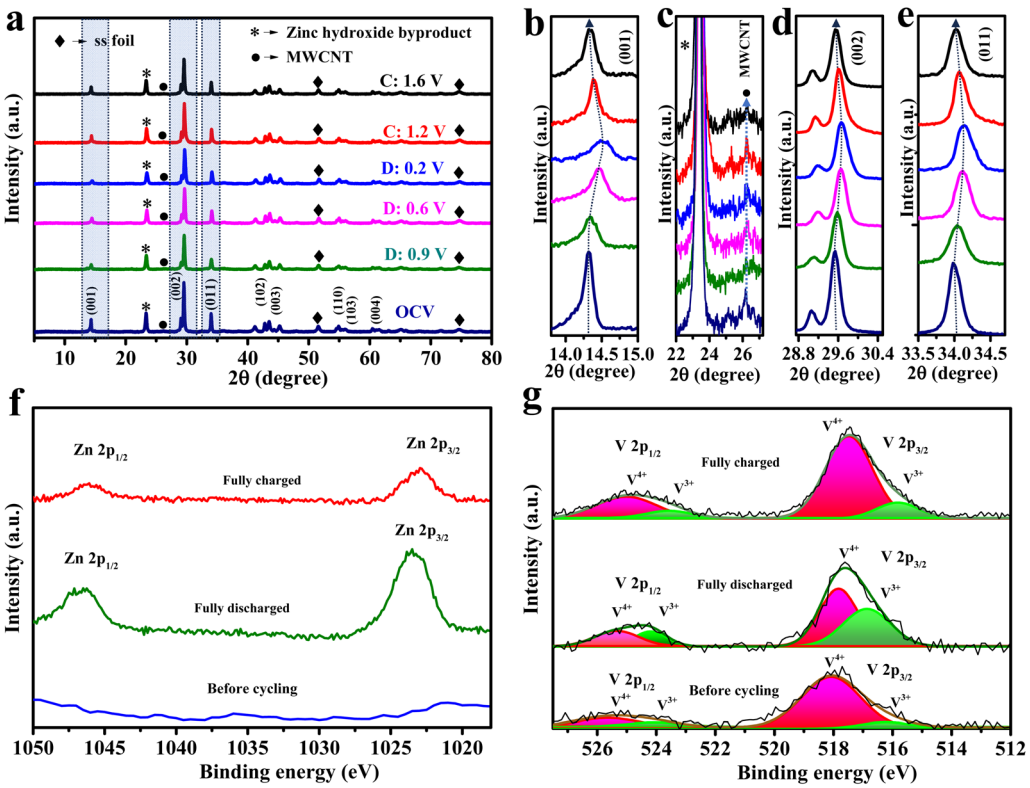

Fig. 6 (a) *Ex situ* XRD plots of VSe_2–MWCNT at different charge states. (b)–(e) Magnified *ex situ* XRD plots corresponding to the (001) plane, MWCNT and zinc hydroxide byproduct, (002) plane, and (011) plane, respectively. (f) Comparison of the XPS spectra of VSe_2–MWCNT in the charged and discharged states. (g) Deconvoluted V 2p XPS spectra in the charged and discharged states.

© 2025 The Author(s). Published by the Royal Society of Chemistry

Open Access Article. Published on 28 July 2025. Downloaded on 4/13/2026 6:53:46 PM.
This article is licensed under a Creative Commons Attribution 3.0 Unported Licence.

shifts. In particular, the peak for the MWCNTs also shifts to a lower angle due to residual Zn-ion intercalation during the charge/discharge process. The sequential shift and recovery of XRD peaks indicate that the VSe_2 can accommodate and release Zn ions without complete structural collapse, which is favourable for long-term stability. The chemical changes associated with vanadium during Zn-ion storage were further studied using *ex situ* XPS, and the results are shown in Fig. 6f and g. Zn 2p peaks are not present in the VSe_2 cathode before cycling, but emerge during the discharge process, indicating the intercalation of Zn-ions into the VSe_2 structure. The Zn-ions are stored *via* the reduction of V and change in the environment of Se, and the two peaks at ~1023 eV and ~1046 eV corresponding to Zn $2p_{1/2}$ and Zn $2p_{3/2}$ confirm that the Zn-ions are stored as Zn_xVSe_2; no formation of Zn_0 is noted. Upon consecutive charging, less-intense characteristic Zn 2p peaks were still observed, indicating that the Zn-ions were not fully recovered during the consecutive charge process. The Zn^{2+} ions could become trapped in the VSe_2 layers and in the defects, making them detectable in the XPS spectrum. However, this could reduce the amount of active sites available for zinc ion intercalation, thereby decreasing ion accessibility and transport within the cathode material. This could also be attributed to the formation of a zinc-species-containing stable interfacial layer over the cathode.[64] This type

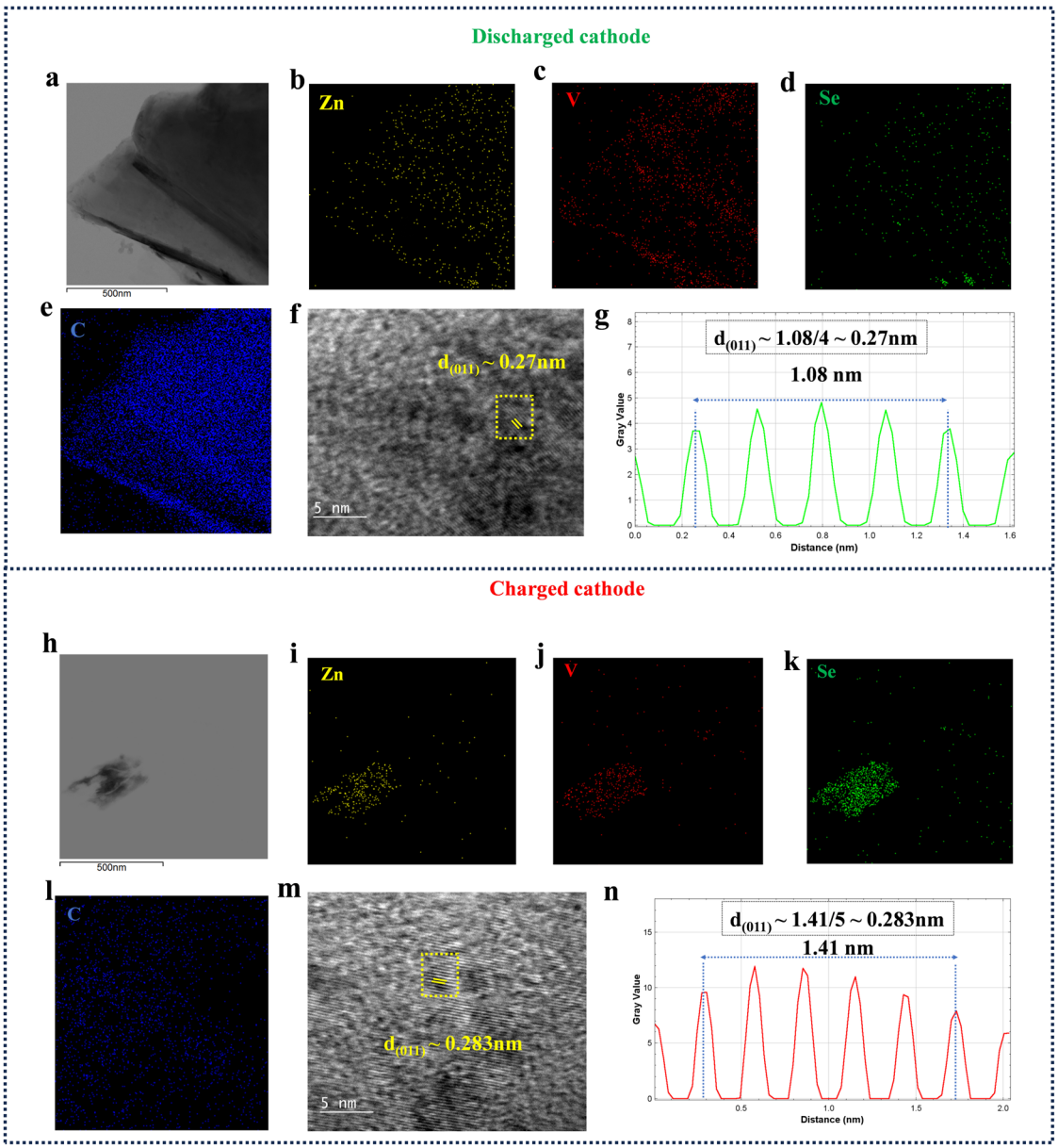

Fig. 7 (a) FETEM image of the discharged VSe_2@MWCNT cathode, (b–e) HAADF elemental mapping of the discharged VSe_2@MWCNT cathode, (f) HRTEM image of the discharged VSe_2@MWCNT cathode, (g) corresponding gray value *vs.* interplanar spacing plot, (h) FETEM image of the charged VSe_2@MWCNT cathode, (i–l) HAADF elemental mapping of the charged VSe_2@MWCNT cathode, (m) HRTEM image of the charged VSe_2@MWCNT cathode, and (n) corresponding gray value *vs.* interplanar spacing plot.

Open Access Article. Published on 28 July 2025. Downloaded on 4/13/2026 6:53:46 PM. This article is licensed under a Creative Commons Attribution 3.0 Unported Licence.

of behaviour has been observed in many vanadium-based oxides and selenides.

The deconvoluted V 2p spectrum before cycling shows the dominant nature of the V^{4+} state in VSe_2 along with a small amount of V^{3+} due to defects in the layered structure.[20] Upon discharging, the intensity of V^{4+} was significantly reduced with an increase in the V^{3+} region, indicating that the Zn-ion storage takes place through the reduction of V^{4+} to V^{3+}. Upon consecutive charging, the valence state of V returns to the initial V^{4+}, indicating good reversibility.[20,63] The full width at half maximum (FWHM) values were calculated for the cathodes in the charged, discharged, and pristine states, as shown in Table S2. The intercalation of zinc ions into the VSe_2 layers causes the vanadium to be reduced from the V^{4+} valence state to V^{3+}, creating a more homogeneous chemical environment. This results in sharper V 2p peaks and a decreased FWHM. During charging, the material exhibits mixed valence states along with unwanted surface reactions and chemical disorder, which cause broadening of the V 2p peaks and an increased FWHM.[65,66]

The change in the VSe_2 lattices during Zn-ion storage was evaluated using *ex situ* HRTEM and HAADF analysis. Fig. 7 provides a good understanding of the structural reversibility and distribution of intercalated Zn-ions in the VSe_2 layers during the charge and discharge process. In the discharged state, the uniform distribution of Zn-ions over the VSe_2 cathode is clearly observed through HAADF mapping, which shows an even distribution of Zn along with V, Se and C. The interplanar spacing for the (011) plane for Zn-ion intercalated VSe_2 was calculated from the gray value *d*-spacing plot, and was found to have decreased to $\sim$0.27 from 0.3 nm, confirming the intercalation of Zn-ions into the layered structure. After consecutive charging, the distribution of Zn-ions in the VSe_2 cathode was significantly reduced, indicating the removal of the Zn-ions. However, a slight amount of Zn-ions was distributed over the cathode due to irreversibility, confirming the results of the previous XPS study. The interplanar spacing of the VSe_2 cathode returned to almost its original value ($\sim$0.27 nm to $\sim$0.283 nm) for the (011) plane, confirming good structural reversibility for Zn-ion storage in VSe_2. The combined findings of *ex situ* XRD, *ex situ* XPS, *ex situ* HRTEM and electrochemical analysis confirm the reversible nature of the VSe_2 cathode for Zn-ion storage. The VSe_2–MWCNT cathode shows prolonged electrochemical stability due to the reversible structural changes during the process. Although an initial Zn-ion irreversibility is observed in the VSe_2 cathode, the stability of the VSe_2–MWCNT nanohybrid is not compromised, as evidenced by its ultra-long-term stability towards Zn-ion storage. The detailed mechanism of charge storage in the two-dimensional VSe_2 layers during the charging and discharging processes can be given as:

$$VSe_2\text{–MWCNT} + xZn^{2+} + 2xe^- \leftrightarrow Zn_xVSe_2\text{–MWCNT}$$

The two-dimensional framework of the VSe_2 enables rapid and reversible redox-mediated Zn-ion storage with more active sites unlocked for Zn ion adsorption. The 2D layered architecture of VSe_2 along with the nano-carbon support facilitates ultra-fast pseudocapacitive-mediated Zn-ion storage, which plays a crucial role in the remarkable charge storage performance of VSe_2. The strong metallic characteristic of the VSe_2–MWCNT nano-hybrid arising synergistically from the 2D VSe_2 and MWCTNs, along with the robust 2D layered structure, facilitated the achievement of high capacity, high rate performance and good stability in VSe_2 as a cathode for Zn-ion batteries. Interestingly, the VSe_2 cathode exhibited more facile and rapid Zn-ion storage than several previously studied metal–oxide-, polyanion-, and metal–sulphide-based cathodes for Zn-ion batteries.

4. Conclusion

In summary, a 2D VSe_2–MWCNT nanohybrid with a favourable layered structure was investigated as an effective cathode material for aqueous zinc-ion batteries. The transition-metal–chalcogenide-based cathode with strong metallic characteristics and defects exhibited ultra-fast pseudocapacitive-type storage to deliver high discharge capacity, superior rate performance, and robust stability. The nano-hybrid cathode can reversibly store zinc-ions after initial structural stabilization to achieve a discharge capacity of 214 mAh g^{-1} at 0.2 A g^{-1} and long-term cycling with 98% capacity retention at 1 A g^{-1} after 600 cycles. Several *ex situ* characterisations revealed reversible structural changes in the crystal structure along with fast zinc-ion diffusion inside the 2D layered cathode, which was superior to metal oxides/sulfides for achieving high-rate zinc-ion batteries. The effective design strategy of advanced TMD cathode materials could provide outstanding rate performance and long-term cycling for aqueous zinc ion batteries, which are suitable for large-scale energy storage technologies. The current study presents such an effective design strategy for transition-metal–selenide-based cathode materials with pseudocapacitive-type storage for multivalent aqueous batteries with high capacity and outstanding rate and stability.

Conflicts of interest

There is no conflict of interest to declare.

Data availability

Both physical and electrochemical characterizations, for physical characterization the TGA plot, FESEM and TEM images have provided, in the electrochemical section GCD for Pristine VSe_2, Nyquist plot with its equivalent circuit, and plots showing capacitive and diffusive contributions for pristine VSe_2, pristine MWCNT and their physical mixture have been included. See DOI: https://doi.org/10.1039/d5ya00130g

Data will be made available upon request from the authors.

© 2025 The Author(s). Published by the Royal Society of Chemistry

Open Access Article. Published on 28 July 2025. Downloaded on 4/13/2026 6:53:46 PM. This article is licensed under a Creative Commons Attribution 3.0 Unported Licence.

Acknowledgements

Dr. Ranjith Thangavel acknowledges the support from the CPRI Bangalore under the Ministry of Power, Government of India through NPP scheme (NPP/21-26/GD/4), and Anusandhan National Research Foundation (ANRF), a statutory body of the Department of Science & Technology (DST), Govt. of India, through the project number: CRD/2024/000715.

References

1 N. Zhang, X. Chen, M. Yu, Z. Niu, F. Cheng and J. Chen, *Chem. Soc. Rev.*, 2020, **49**, 4203–4219.
2 T. Wang, C. Li, X. Xie, B. Lu, Z. He, S. Liang and J. Zhou, *ACS Nano*, 2020, **14**, 16321–16347.
3 L. Chen, Q. An and L. Mai, *Adv. Mater. Interfaces*, 2019, **6**, 1900387.
4 X. Zhao, X. Liang, Y. Li, Q. Chen and M. Chen, *Energy Storage Mater.*, 2021, **42**, 533–569.
5 N. Mohamed and N. K. Allam, *RSC Adv.*, 2020, **10**, 21662–21685.
6 W. Lee, S. Muhammad, C. Sergey, H. Lee, J. Yoon, Y. M. Kang and W. S. Yoon, *Angew. Chem., Int. Ed.*, 2020, **59**, 2578–2605.
7 M. Devi, B. Moorthy and R. Thangavel, *Sustainable Energy Fuels*, 2023, **7**, 3776–3795.
8 H. Shuai, R. Liu, W. Li, X. Yang, H. Lu, Y. Gao, J. Xu and K. Huang, *Adv. Energy Mater.*, 2023, **13**, 2202992.
9 K. Yang, Y. Hu, T. Zhang, B. Wang, J. Qin, N. Li, Z. Zhao, J. Zhao and D. Chao, *Adv. Energy Mater.*, 2022, **12**, 2202671.
10 X. Ma, X. Cao, M. Yao, L. Shan, X. Shi, G. Fang, A. Pan, B. Lu, J. Zhou and S. Liang, *Adv. Mater.*, 2022, **34**, 2105452.
11 Z. Liu, R. Wang, Q. Ma, J. Wan, S. Zhang, L. Zhang, H. Li, Q. Luo, J. Wu, T. Zhou and J. Mao, *Adv. Funct. Mater.*, 2024, **34**, 2214538.
12 M. Song, H. Tan, D. Chao and H. J. Fan, *Adv. Funct. Mater.*, 2018, **28**, 1802564.
13 B. Wu, G. Zhang, M. Yan, T. Xiong, P. He, L. He, X. Xu and L. Mai, *Small*, 2018, **14**, 1703850.
14 Y. An, Y. Tian, Q. Man, H. Shen, C. Liu, Y. Qian, S. Xiong, J. Feng and Y. Qian, *ACS Nano*, 2022, **16**, 6755–6770.
15 Y. Zhang, F. Wan, S. Huang, S. Wang, Z. Niu and J. Chen, *Nat. Commun.*, 2020, **11**, 2199.
16 T. Zhou, L. Zhu, L. Xie, Q. Han, X. Yang, L. Chen, G. Wang and X. Cao, *J. Colloid Interface Sci.*, 2022, **605**, 828–850.
17 L. Zhu, P. Ge, L. Xie, Y. Miao and X. Cao, *Electrochem. Commun.*, 2020, **115**, 1067.
18 X. Jia, C. Liu, Z. G. Neale, J. Yang and G. Cao, *Chem. Rev.*, 2020, **120**, 7795–7866.
19 W. Liu, J. Hao, C. Xu, J. Mou, L. Dong, F. Jiang, Z. Kang, J. Wu, B. Jiang and F. Kang, *Chem. Commun.*, 2017, **53**, 6872–6874.
20 Y. Bai, H. Zhang, B. Xiang, X. Liang, J. Hao, C. Zhu and L. Yan, *ACS Appl. Mater. Interfaces*, 2021, **13**, 23230–23238.
21 P. He, M. Yan, G. Zhang, R. Sun, L. Chen, Q. An and L. Mai, *Adv. Energy Mater.*, 2017, **7**, 1700464.
22 R. Zhang, C. Pan, R. G. Nuzzo and A. A. Gewirth, *J. Phys. Chem. C*, 2019, **123**, 8740–8745.
23 Y. Tang, X. Li, H. Lv, D. Xie, W. Wang, C. Zhi and H. Li, *Adv. Energy Mater.*, 2020, **10**, 2000892.
24 Y. Jin, M. E. Lee, G. Kim, H. Seong, W. Nam, S. K. Kim, J. H. Moon and J. Choi, *Materials*, 2023, **16**, 1253.
25 M. Yan, X. Pan, P. Wang, F. Chen, L. He, G. Jiang, J. Wang, J. Z. Liu, X. Xu, X. Liao and J. Yang, *Nano Lett.*, 2017, **17**, 4109–4115.
26 A. V. Murugan, C. S. Gopinath and K. Vijayamohanan, *Electrochem. Commun.*, 2005, **7**, 213–218.
27 Q. Li, W. Zhang, J. Peng, D. Yu, Z. Liang, W. Zhang, J. Wu, G. Wang, H. Li and S. Huang, *Adv. Funct. Mater.*, 2022, **32**, 2112776.
28 M. Rani, M. Sehrawat, S. Sharma and B. P. Singh, *J. Energy Storage*, 2023, **73**, 109063.
29 K. K. Gangu, S. Maddila, S. B. Mukkamala and S. B. Jonnalagadda, *J. Energy Chem.*, 2019, **30**, 132–144.
30 P. Siddu, S. R. KA, S. Radhakrishnan, S. M. Jeong and C. S. Rout, *Batteries Supercaps*, 2025, **8**, e202400466.
31 A. S. Sree, B. Shajahan, B. Chakraborty and C. S. Rout, *RSC Adv.*, 2020, **10**, 31712–31719.
32 M. Narayanasamy, L. Hu, B. Kirubasankar, Z. Liu, S. Angaiah and C. Yan, *J. Alloys Compd.*, 2021, **882**, 160704.
33 G. D. Park, J. H. Kim, S. K. Park and Y. C. Kang, *ACS Appl. Mater. Interfaces*, 2017, **9**, 10673–10683.
34 L. Wang, Z. Wu, M. Jiang, J. Lu, Q. Huang, Y. Zhang, L. Fu, M. Wu and Y. Wu, *J. Mater. Chem. A*, 2020, **8**, 9313–9321.
35 W. Oh, H. Park, B. S. Jin, R. Thangavel and W. S. Yoon, *J. Mater. Chem. A*, 2020, **8**, 10331–10336.
36 R. Thangavel, D. Han, B. Moorthy, B. K. Ganesan, M. Moorthy, Y. Park, K. W. Nam and Y. S. Lee, Small, *Methods*, 2022, **6**, 2100888.
37 Z. Wu, C. Lu, Y. Wang, L. Zhang, L. Jiang, W. Tian, C. Cai, Q. Gu, Z. Sun and L. Hu, *Small*, 2020, **16**, 2000698.
38 T. G. Park, B. K. Choi, J. Park, J. Kim, Y. J. Chang and F. Rotermund, *ACS Nano*, 2021, **15**, 7756–7764.
39 V. Soundharrajan, S. Nithiananth, J. Lee, K. Sakthiabirami, D. T. Pham, J. H. Kim, J. Y. Hwang and J. Kim, *J. Power Sources*, 2023, **558**, 232542.
40 D. Xie, Y. Sang, D. H. Wang, W. Y. Diao, F. Y. Tao, C. Liu, J. W. Wang, H. Z. Sun, J. P. Zhang and X. L. Wu, *Angew. Chem., Int. Ed.*, 2023, **62**, e202216934.
41 L. Chen, Q. An and L. Mai, *Adv. Mater. Interfaces*, 2019, **6**, 1900387.
42 S. Li, P. Das, X. Wang, C. Li, Z. S. Wu and H. M. Cheng, *Small*, 2025, 2410036.
43 H. Lu, J. Hu, Y. Zhang, K. Zhang, X. Yan, H. Li, J. Li, Y. Li, J. Zhao and B. Xu, *Adv. Mater.*, 2023, **35**, 2209886.
44 W. Cui, J. Wang, Y. Li, P. Liu and F. Dong, *Environ. Sci.: Nano*, 2025, **12**, 67–97.
45 L. Wang, Z. Wu, M. Jiang, J. Lu, Q. Huang, Y. Zhang, L. Fu, M. Wu and Y. Wu, *J. Mater. Chem. A*, 2020, **8**, 9313–9321.
46 X. Chen, X. Hu, Y. Chen, X. Cao, Y. Huang, H. Zhang, J. H. Liu, Y. Wang, S. L. Chou and D. Cao, *J. Mater. Chem. A*, 2022, **10**, 22194–22204.

© 2025 The Author(s). Published by the Royal Society of Chemistry

Open Access Article. Published on 28 July 2025. Downloaded on 4/13/2026 6:53:46 PM.
This article is licensed under a Creative Commons Attribution 3.0 Unported Licence.

47 X. Zhu, W. Wang, Z. Cao, S. Gao, M. O. L. Chee, X. Zhang, P. Dong, P. M. Ajayan, M. Ye and J. Shen, *J. Mater. Chem. A*, 2021, **9**, 17994–18005.
48 Q. Liu, K. Yang, Z. Wang, S. Chen, W. Zhang, H. Ma, X. Geng, Q. Deng, Q. Zhao and N. Zhu, *ACS Appl. Mater. Interfaces*, 2024, **16**, 20610–20617.
49 G. Li, L. Sun, S. Zhang, C. Zhang, H. Jin, K. Davey, G. Liang, S. Liu, J. Mao and Z. Guo, *Adv. Funct. Mater.*, 2024, **34**, 2301291.
50 X. Cui, Y. Li, Y. Zhang, Z. Sun, Y. Liu, J. Zhang, E. Xie and J. Fu, *Chem. Eng. J.*, 2023, **478**, 147197.
51 V. Soundharrajan, S. Nithiananth, J. Lee, J. H. Kim, J. Y. Hwang and J. Kim, *J. Mater. Chem. A*, 2022, **10**, 18162–18169.
52 V. Soundharrajan, J. Lee, S. Kim, J. H. Kim, J. Y. Hwang and J. Kim, *Batteries Supercaps*, 2023, **6**, e202200527.
53 J. Jiang, H. Li, J. Huang, K. Li, J. Zeng, Y. Yang, J. Li, Y. Wang, J. Wang and J. Zhao, *ACS Appl. Mater. Interfaces*, 2017, **9**, 28486–28494.
54 Y. Gao, H. Yang, X. Wang, Y. Bai, N. Zhu, S. Guo, L. Suo, H. Li, H. Xu and C. Wu, *ChemSusChem*, 2020, **13**, 732–740.
55 L. Geng, J. P. Scheifers, C. Fu, J. Zhang, B. P. T. Fokwa and J. Guo, *ACS Appl. Mater. Interfaces*, 2017, **9**, 21251–21257.
56 Q. Pang, S. Yang, X. Yu, W. He, S. Zhang, Y. Tian, M. Xing, Y. Fu and X. Luo, *J. Alloys Compd.*, 2021, **885**, 161008.
57 X. Yang, Q. Sun, L. Chai, S. Chen, W. Zhang, H. Y. Yang and Z. Li, *Small*, 2024, **20**, 2400335.
58 Y. Bai, H. Zhang, H. Song, C. Zhu, L. Yan, Q. Hu and C. M. Li, *Nano Energy*, 2024, **120**, 109090.
59 J. H. Jo, Y. Aniskevich, J. Kim, J. U. Choi, H. J. Kim, Y. H. Jung, D. Ahn, T.-Y. Jeon, K. S. Lee, S. H. Song, H. Kim, G. Ragoisha, A. Mazanik, E. Streltsov and S. T. Myung, *Adv. Energy Mater.*, 2020, **10**, 2001595.
60 F. Wan, L. Zhang, X. Dai, X. Wang, Z. Niu and J. Chen, *Nat. Commun.*, 2018, **9**, 1656.
61 M. H. Alfaruqi, V. Mathew, J. Song, S. Kim, S. Islam, D. T. Pham, J. Jo, S. Kim, J. P. Baboo, Z. Xiu, K.-S. Lee, Y.-K. Sun and J. Kim, *Chem. Mater.*, 2017, **29**, 1684–1694.
62 R. Thangavel, A. Samuthira Pandian, H. V. Ramasamy and Y. S. Lee, *ACS Appl. Mater. Interfaces*, 2017, **9**, 40187–40196.
63 Y. Yi, X. Du, Z. Zhao, Y. Liu, H. Guan, X. Liu, X. Pei, S. Zhang and D. Li, *ACS Nano*, 2022, **16**, 7772–7782.
64 W. Kukułka, V. Montes-García, S. Sarwar, D. Pakulski, P. Samorì and A. Ciesielski, *J. Mater. Chem. A*, 2025, **13**, 22755.
65 Y. Li, C. Zhao, A. Abdukader and X. Wu, *RSC Adv.*, 2024, **14**, 9594–9601.
66 J. Światowska-Mrowiecka, V. Maurice, S. Zanna, L. Klein and P. Marcus, *Electrochim. Acta*, 2007, **52**, 5644–5653.

© 2025 The Author(s). Published by the Royal Society of Chemistry